

Modeling of microstructure and microsegregation evolution in solidification of ternary alloys

Qiannan Yu(于芊楠), Mengdan Hu(胡梦丹), Jinyi Wu(吴津仪), and Dongke Sun(孙东科)

Citation : Chin. Phys. B, 2025, 34 (**5**): 056801. DOI: 10.1088/1674-1056/adb8b5
http://cpb.iphy.ac.cn; http://iopscience.iop.org/cpb

What follows is a list of articles you may be interested in

Effects of WC-Co reinforced Ni-based alloy by laser melting deposition: Wear resistance and corrosion resistance

Zhao-Zhen Huang(黄昭祯), Zhi-Chen Zhang(张志臣), Fan-Liang Tantai(澹台凡亮), Hong-Fang Tian(田洪芳), Zhen-Jie Gu(顾振杰), Tao Xi(郗涛), Zhu Qian(钱铸), and Yan Fang(方艳)
Chin. Phys. B, 2021, 30 (**1**): 016802. DOI: 10.1088/1674-1056/abb223

Segregation behavior and embrittling effect of lanthanide La, Ce, Pr, and Nd at Σ3(111) tilt symmetric grain boundary in α-Fe

Jinli Cao(曹金利), Wen Yang(杨文), Xinfu He(贺新福)
Chin. Phys. B, 2019, 28 (**12**): 126802. DOI: 10.1088/1674-1056/ab5277

Segregations and desorptions of Ge atoms in nanocomposite $Si_{1-x}Ge_x$ films during high-temperature annealing

Yu Wang(汪煜), Meng Yang(杨濛), Gang Wang(王刚), Xiao-Xu Wei(魏晓旭), Jun-Zhuan Wang(王军转), Yun Li(李昀), Ze-Wen Zou(左则文), You-Dou Zheng(郑有炓), Yi Shi(施毅)
Chin. Phys. B, 2017, 26 (**12**): 126801. DOI: 10.1088/1674-1056/26/12/126801

Structural, optical, and electrical properties of Cu-doped ZrO_2 films prepared by magnetron co-sputtering

Nian-Qi Yao(姚念琦), Zhi-Chao Liu(刘智超), Guang-Rui Gu(顾广瑞), Bao-Jia Wu(吴宝嘉)
Chin. Phys. B, 2017, 26 (**10**): 106801. DOI: 10.1088/1674-1056/26/10/106801

Effects of the $Be_{22}W$ phase formation on hydrogen retention and blistering in mixed Be/W systems

Jin-Li Cao(曹金利), Bing-Ling He(赫丙龄), Wei Xiao(肖伟), Li-Gen Wang(王立根)
Chin. Phys. B, 2017, 26 (**7**): 076801. DOI: 10.1088/1674-1056/26/7/076801

Modeling of microstructure and microsegregation evolution in solidification of ternary alloys

Qiannan Yu(于芊楠)[1,2,3], Mengdan Hu(胡梦丹)[1,2,3], Jinyi Wu(吴津仪)[1,2,3], and Dongke Sun(孙东科)[1,2,3,†]

[1] *School of Mechanical Engineering, Southeast University, Nanjing* 211189, *China*
[2] *Jiangsu Key Laboratory for Biomaterials and Devices, Southeast University, Nanjing* 211189, *China*
[3] *Key Laboratory of Structure and Thermal Protection of High Speed Aircraft, Ministry of Education, School of Mechanical Engineering, Southeast University, Nanjing* 211189, *China*

(Received 18 December 2024; revised manuscript received 17 February 2025; accepted manuscript online 21 February 2025)

The microstructure formed during solidification has a significant impact on the mechanical properties of materials. In this study, a two-dimensional (2D) cellular automaton (CA)-finite difference (FD)-CALPHAD model was developed to simulate the formation of microstructure and solute segregation in the solidification processes of ternary alloys. In the model, dendritic growth is simulated using the CA technique, while solute diffusion is solved by the FD method, and the CALPHAD method is employed to calculate thermodynamic phase equilibrium during solidification. The CA-FD-CALPHAD coupled model is capable of reproducing the evolution of continuous nucleation and growth of grains as well as the evolution of the microstructure and solute distribution during solidification of ternary alloys. In this study, Al–Zn–Mg ternary alloy is taken as an example to simulate the growth of equiaxed and columnar grains and the columnar-to-equiaxed transition (CET) under different solidification conditions. The simulation results are compared with experimental data from the literature, showing a good agreement. Besides, the study also investigates the evolution of temperature and multicomponent solute fields during solidification and the effects of alloy composition and cooling rate on the microstructure morphology. The results reveal that the initial alloy composition and cooling rate significantly affect dendritic morphology and solute segregation. Higher initial alloy concentrations promote the growth of side branches in equiaxed grains, leading to more pronounced solute segregation between dendrites. As the cooling rate increases, the average grain size of the equiaxed grains decreases accordingly. Additionally, a higher cooling rate accelerates the columnar-to-equiaxed transition, leading to a finer grain structure.

Keywords: ternary alloys, solidification, dendrite, columnar-to-equiaxed transition, cellular automaton

PACS: 68.55.A–, 68.08.De, 81.30.Fb, 81.10.–h

DOI: 10.1088/1674-1056/adb8b5 **CSTR:** 32038.14.CPB.adb8b5

1. Introduction

Aluminum alloys are increasingly critical in industries such as aerospace, automotive, and construction due to their favorable mechanical properties, corrosion resistance, and low density. During manufacturing processes, including casting, welding, and additive manufacturing, the solidification stage is unavoidable. The microstructure formed during these processes directly influences the final properties of the alloy.[1] A comprehensive understanding and precise control of microstructure evolution are essential for producing high-performance materials. Specifically, various solidification conditions impact the characteristics of the final microstructure,[2] including growth morphologies such as equiaxed or columnar dendrites, as well as micro-segregation. During the formation of microstructure, the solutes of different elements are redistributed, leading to micro-segregation. Furthermore, the columnar-to-equiaxed transition (CET) occurs when equiaxed grains ahead of the columnar growth front obstruct further columnar grain growth. Both the columnar-to-equiaxed grain ratio[3] and the severity of segregation[4] play a significant role in determining material properties.

Over the past few decades, the solidification behavior of aluminum alloys under various solidification conditions has garnered significant attention from scientists and engineers. Numerous studies have been conducted to investigate the mechanisms of microstructure evolution using experimental approaches. Numerous studies have been conducted to investigate the mechanisms of microstructure evolution using experimental approaches. Optical microscopy (OM) and scanning electron microscopy (SEM) serve as crucial tools for the observation and in-depth analysis of solidification.[5] Advances in x-ray imaging technologies have greatly improved our understanding of microstructural evolution during dendritic solidification. The heterogeneous nucleation process,[6] growth of both equiaxed and columnar grains,[7] and CET dynamics in metallic alloys[7,8] have been investigated using x-ray techniques. Despite these advancements, experimental methods face limitations related to resolution, melting points, and alloy size, making them labor-intensive and time-consuming. Consequently, capturing the complete microstructural evolution in real-time remains a significant challenge for experimental ap-

[†]Corresponding author. E-mail: dksun@seu.edu.cn

© 2025 Chinese Physical Society and IOP Publishing Ltd. All rights, including for text and data mining, AI training, and similar technologies, are reserved.

proaches.

The rapid advancement in computational technology has enabled the application of various numerical methods, such as the phase-field (PF) and cellular automaton (CA) models, to investigate the solidification process of alloys. The phase-field method overcomes the challenges of tracking the liquid-solid interface by establishing phase-field equations.[9] Additionally, this method allows for the integration of temperature fields, solute fields, flow fields, and other external factors, facilitating a realistic simulation of complex dendritic morphologies and their evolution. Recently, Zhang *et al.*[10] simulated the growth of single and multiple Mg–Gd dendrites under convection and systematically investigated the effects of factors such as orientation angle, flow intensity, and undercooling on dendrite morphology. Zhu *et al.*[11] conducted simulations to investigate the competitive growth and evolution of columnar grains during directional solidification. They quantitatively analyzed the influence of parameters, including pulling velocity and anisotropy strength, on the morphological evolution of dendritic growth. Mao *et al.*[12] modelled the growth and movement of dendrites during non-equilibrium solidification of Ni–Nb alloys. The transformation process from equiaxed to columnar crystals was reproduced, and the microstructure and segregation within the PDAS and local regions were quantitatively investigated. However, due to the complexity of phase-field equations and the limitations in data processing capacity of computers, phase-field simulations remain restricted to small domains.[13]

Compared to the PF method, CA models are particularly appealing due to their simple algorithm structure[14] and the ability to simulate complex phenomena with acceptable computation resources.[15] Microstructure simulation models based on the CA technique can replicate most experimentally observed dendritic features with reasonable computational efficiency. For example, Zhang *et al.*[16] simulated the two-dimensional solidification of an Al–3 wt% Cu alloy, encompassing the growth and movement of single and multiple equiaxed crystals in a flow and subsequent grain growth during the CET. Furthermore, a three-dimensional large-scale CA model was proposed by Zhang *et al.*[17] to simulate isothermal and directional solidification in Fe–C alloys, including the CET. The directional solidification structures under different cooling rates were obtained through simulation. While the aforementioned studies primarily focus on binary alloys, real-world alloys often involve multiple components, posing significant challenges for simulation. In addressing the problem, Tan *et al.*[18] established an improved CA model to simulate the growth of multiple equiaxed grains in ternary Al–Si–Mg alloys and explored the effects of cooling rate on secondary dendrite arm spacing (SDAS) and grain size. Gu *et al.*[19] extended the model to calculate the solidification process of a five-component alloy, simulating the directional solidification of an Al–Si–Mg–Fe–Mn alloy.

Among the various solidification processes, the study of molten pool solidification is particular significance due to its direct impact on advanced manufacturing techniques such as additive manufacturing and welding. The molten pool is a highly dynamic region where solidification occurs under complex thermal conditions. Rapid variations in the temperature field during solidification cause uneven solute distribution, leading to solute segregation. The element segregation phenomenon can result in compositional heterogeneity and localized microstructural differences, thereby directly affecting the performance and reliability of the AM-fabricated components.[20,21] Therefore, molten pool solidification is essential for advancing fundamental knowledge of solidification mechanisms, optimizing process parameters, and driving the development of high-performance materials and cutting-edge manufacturing technologies.[22,23] Efforts have also been made to predict solidification behavior in molten pools. The coupled CA-FE model was employed by Sheng *et al.*[24] to simulate the microstructural evolution of solidification in different regions and to quantitatively compare the average grain size. Similarly, Xiong *et al.*[25] applied the CA method to simulate the grain structure in the molten zone of Ti6Al4V. The simulated grain morphology and average grain size were in good agreement with experimental results. An *et al.*[26] focused on the solidification process of Inconel 625 formers, simulating and analyzing the temperature field evolution. Their work reproduced the grain growth process and final morphology in both the X–Y and Y–Z cross-sections of the molten pool.

Although progress has been made in simulating solidification in multicomponent alloys, the scope remains relatively limited. Many studies assume fixed numbers and positions for nuclei, focusing either on equiaxed growth or directional solidification of columnar grains while neglecting the continuous nucleation process. Furthermore, most simulations of molten pools emphasize microstructural morphology evolution, with insufficient attention to solute distribution. So far, few studies have comprehensively considered continuous grain nucleation and growth, the occurrence of CET, and solute distribution during the solidification of ternary alloys. In the present work, a CA–FD–CALPHAD coupled model is proposed to simulate the nucleation and growth of dendritic grains in the ternary Al–Zn–Mg alloy system. This model effectively captures the morphological changes and concentration variations of dendrites.

2. Model description

In this work, the solidification process of ternary Al–Zn–Mg alloys is simulated using the cellular automaton (CA)

method. The computational domain is divided into a uniform quadrilateral grid, with the smallest computational unit referred to as a cell. Each cell is characterized by several variables (such as temperature, concentration, and solid fraction) and states (solid or liquid). The cellular automaton evolves in discrete time steps, continuously calculating the values of the cell variables and updating their states according to predefined capture rules. The quantitative information on multiphase equilibria in Al–Zn–Mg alloy systems is obtained using PanEngine, a multi-component phase equilibrium computation engine based on the CALPHAD method.[27,28] To enhance computational performance, a data tabulation coupling approach between PanEngine and CA is employed.[29]

2.1. Temperature field

The governing equation for calculating the temperature distribution, excluding latent heat of solidification, is given by

$$\rho C_{\mathrm{p}} \frac{\partial T}{\partial t} = \nabla \cdot (\lambda \nabla T). \tag{1}$$

With latent heat of solidification, the governing equation for calculating the temperature distribution is given by

$$\rho C_{\mathrm{p}} \frac{\partial T}{\partial t} = \nabla \cdot (\lambda \nabla T) + \rho L \frac{\partial f_{\mathrm{s}}}{\partial t}, \tag{2}$$

where T is temperature, t is time, ρ is density, C_{p} is specific heat, λ is thermal conductivity, f_{s} is solid fraction, and L is the latent heat of solidification.

2.2. Nucleation and growth of dendrites

The continuous model is employed to describe the inhomogeneous nucleation phenomenon in the melt, where nucleation occurs continuously throughout the solidification process, rather than instantaneously at a single point in time. In this study, both nucleation and grain growth are driven by the undercooling at the solid/liquid interface. The increase in nucleation density ($\mathrm{d}n$) is induced by an increase in undercooling ($\mathrm{d}(\Delta T)$), following a Gaussian distribution

$$\frac{\mathrm{d}n}{\mathrm{d}(\Delta T)} = \frac{n_{\max}}{\sqrt{2\pi}\Delta T_\sigma} \exp\left[-\frac{1}{2}\left(\frac{\Delta T - \Delta T_{\max}}{\Delta T_\sigma}\right)^2\right], \tag{3}$$

where $\Delta T_{\max}$ is the mean nucleation undercooling, ΔT_σ is the standard deviation, and $n_{\max}$ is the maximum density of nuclei. These three nucleation parameters are influenced by the alloy composition and process variables.

Thus, the nucleation density $n(\Delta T)$ is given by

$$n(\Delta T) = \int_0^{\Delta T} \frac{\mathrm{d}n}{\mathrm{d}(\Delta T)} \mathrm{d}(\Delta T). \tag{4}$$

In a discrete time step Δt, the temperature decreases by δT, and undercooling accordingly increases by $\delta(\Delta T)$. The nucleation density in one time step can be calculated using the following formula:

$$\delta n = \int_{\Delta T}^{\Delta T + \delta(\Delta T)} \frac{\mathrm{d}n}{\mathrm{d}(\Delta T)} \mathrm{d}(\Delta T) = n(\Delta T + \delta(\Delta T)) - n(\Delta T). \tag{5}$$

Given that the computational domain is two-dimensional, the number of newly formed grains can be calculated as $\delta N = \delta n \cdot S$, where S is the area of the computational domain, and δN is the new grain number.

At the beginning of the simulation, the computational domain is filled with molten liquid with a uniform initial alloy composition, and each cell has the same initial undercooling. The initial nucleation number can be calculated according to the Gaussian distribution given by Eq. (3). A corresponding number of cells are randomly selected as nuclei, with their phase changing from liquid to solid. Nuclei are randomly assigned a crystallographic orientation.

The cells selected as nuclei are activated and begin to grow when the temperature falls below the liquidus temperature, reaching the undercooling threshold for nucleation. In the present simulation, the growth velocity of a dendrite tip at a certain undercooling is calculated based on the sharp interface model of the Gibbs–Thomson equation. The total undercooling at the solid/liquid interface serves as the driving force for dendrite growth, as given by

$$\Delta T = T^{\mathrm{eq}} - T^* - \bar{\Gamma} \cdot \omega mc, \tag{6}$$

where ΔT represents the total undercooling in the solid/liquid interface, T^{eq} is the equilibrium liquidus temperature of the alloy, T^* is the local temperature at the S/L interface, $\bar{\Gamma}$ is the average Gibbs–Thomson coefficient, and ωmc is the curvature at the S/L interface which accounts for the effects of surface energy anisotropy. This can be calculated as follows:[30]

$$\begin{aligned} \omega mc &= -\nabla \cdot \xi(\boldsymbol{n}) \\ &= (3\varepsilon - 1) \cdot (\partial_x n_x + \partial_y n_y + \partial_z n_z) \\ &\quad - 48\varepsilon \cdot \left(n_x^2 \cdot \partial_x n_x + n_y^2 \cdot \partial_y n_y + n_z^2 \cdot \partial_z n_z\right) \\ &\quad + 12\varepsilon \cdot Q \cdot (\partial_x n_x + \partial_y n_y + \partial_z n_z) \\ &\quad + 12\varepsilon \cdot (n_x \cdot \partial_x Q + n_y \cdot \partial_y Q + n_z \cdot \partial_z Q), \end{aligned} \tag{7}$$

where ξ is the Cahn–Hoffman vector, ε is the degree of anisotropy of the surface energy. $\boldsymbol{n} = \nabla f_{\mathrm{s}}/|\nabla f_{\mathrm{s}}| = n_x \boldsymbol{i} + n_y \boldsymbol{j} + n_z \boldsymbol{k}$ is the normal unit vector at the S/L interface, $n_x = \partial_x f_{\mathrm{s}}/|\nabla f_{\mathrm{s}}|$, $n_y = \partial_y f_{\mathrm{s}}/|\nabla f_{\mathrm{s}}|$, and $n_z = \partial_z f_{\mathrm{s}}/|\nabla f_{\mathrm{s}}|$ represent the component of $\boldsymbol{n}$, Q is defined as $Q = n_x^4 + n_y^4 + n_z^4$, where $|\nabla f_{\mathrm{s}}| = \sqrt{(\partial_x f_{\mathrm{s}})^2 + (\partial_y f_{\mathrm{s}})^2 + (\partial_z f_{\mathrm{s}})^2}$.

Based on the anisotropy function of the interface energy, the growth velocity can be expressed as

$$V = \bar{\mu}\left[\frac{1}{1 + 3\delta - 4\delta\left(n_x^4 + n_y^4 + n_z^4\right)}\right]\Delta T, \tag{8}$$

where $\bar{\mu}$ represents the average interface kinetic coefficient and δ is the degree of the kinetic anisotropy of the alloy. The

increment of the fraction at the interface cell in a certain time step Δt can be calculated as

$$\Delta f = G\frac{V}{\Delta x}\Delta t, \tag{9}$$

where G is the geometrical factor relevant to the state of the S/L neighboring cells, Δx is the size of the cell.

2.3. Solute redistribution

As solidification proceeds, solutes are expelled from the solid phase into the liquid phase at the solid/liquid (S/L) interface, creating a solute gradient and driving solute transport. Under the assumption that melt convection is not considered, solute transport is solely driven by diffusion. According to Fick's law, the governing equation for solute diffusion is given by

$$\frac{\partial C(X)}{\partial t} = \nabla\left(D(f_\mathrm{s})\nabla\left(C(X)/p(f_\mathrm{s})\right)\right), \tag{10}$$

where t is time, X is solute (Zn or Mg), f_s is solid fraction. $C(X)$ and $D(f_\mathrm{s})$ are the average solute concentration in the grid and the diffusion coefficient, calculated by the following equation respectively:

$$C(X) = C_\mathrm{s}(X)f_\mathrm{s} + C_\mathrm{l}(X)(1-f_\mathrm{s}), \tag{11}$$

$$D_X(f_\mathrm{s}) = k_\mathrm{p}^\mathrm{eq}(X)D_{\mathrm{s},X}f_\mathrm{s} + D_{\mathrm{l},X}(1-f_\mathrm{s}), \tag{12}$$

where $C_\mathrm{s}(X)$ and $C_\mathrm{l}(X)$ represent solid-phase and liquid-phase concentration respectively. $k_\mathrm{p}^\mathrm{eq} = C_\mathrm{s}^\mathrm{eq}/C_\mathrm{l}^\mathrm{eq}$ is the solute partition coefficient. C_s^eq and C_l^eq are the equilibrium concentration in solid and liquid phases, respectively. In Eq. (10), $C(X)/p(f_\mathrm{s})$ is used to convert the average concentration of the lattice into an equivalent concentration, ensuring solute equilibrium at the solid/liquid interface. The values of T_α^eq (from Eq. (6)) and C_s^eq, C_l^eq (used to calculate k_p^eq in Eq. (12)) are obtained from PanEngine calculation.

Figure 1 presents the flowchart of the current calculation procedure. For a given alloy system, key parameters such as solute partition coefficients and liquidus slopes are obtained through a combination of interpolation and lookup processes within existing Pandat databases. The equilibrium liquidus temperature, determined through CALPHAD calculations, is utilized to compute the undercooling, which plays a critical role in governing dendritic nucleation and growth. After nucleation and growth, solute redistribution during solidification is simulated using the FD method, with the solute partition coefficient also provided by CALPHAD. Following the update of the status, temperature, and concentration of each cell, the iterative process continues until the solidification process is complete.

To assess the relationship between various solidification parameters and the resulting solidification structure, the average grain size D, the local segregation index c_i^index, and the global segregation index SI_i are proposed. D is used to characterize the microstructure. The average grain size is a critical parameter in materials science, directly influencing an alloy's mechanical properties. Grain size control is an important part of the design and processing of materials since it can result in major increases in toughness, ductility, and strength through solidification processes.[31] The local segregation index c_i^index is introduced to reflect the variation in solute concentration at a microscopic scale, highlighting areas with significant compositional differences in each cell. The global segregation index SI_i provides an overall measurement of segregation across the entire computational domain. The indices are defined as

$$c_i^\mathrm{index} = \frac{c_{\mathrm{mix},i} - c_{0,i}}{c_{0,i}} \times 100, \tag{13}$$

$$SI_i = \frac{1}{V_\mathrm{domain}} \cdot \iiint_{V_\mathrm{domain}} \left|c_i^\mathrm{index}\right| \mathrm{d}V, \tag{14}$$

where i represents different alloy composition.

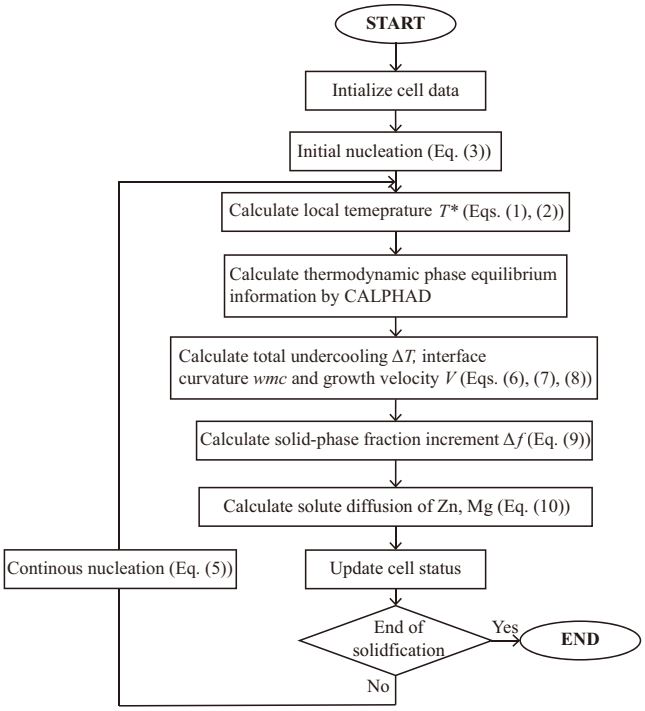


Fig. 1. Flowchart of the solidification simulation procedure by the CA–FD–CALPHAD model.

3. Results and discussion

3.1. Model validation

3.1.1. Mesh-independence verification

To verify the accuracy and stability of the simulation results under different grid resolutions, a mesh independence test is essential. For validation, the number of nuclei formed over a specific time period, the growth velocity and the solute concentration at the tip were used as a benchmark. The temperature field was assumed to be uniform.

Al–Zn–Mg aluminum alloys have significant applications across various industries. Therefore, we take Al–Zn–Mg alloys as a typical object of ternary alloys in this paper. The

relevant physical parameters used in the simulation for Al–Zn–Mg alloys are listed in Table 1.

When performing the mesh-independence test of the nucleation process, the initial undercooling was set to 20 K and the cooling rate was 10 K/s. Nucleation-related parameters were kept constant where $\Delta T_{\max} = 5.0$ K, $\Delta T_\sigma = 2.0$ K, and $n_{\max} = 5.0 \times 10^{14}$ m^{-3}. In the space-step independence test, the physical size of the computational domain remained unchanged. The minimum grid size was set between 0.5 μm and 2.5 μm and the grid number was adjusted according to the grid size. In the time-step independence test, the selection of the time step must satisfy $\Delta t < \Delta x^2/(4.5 \times D_{\mathrm{l,max}})$ to ensure the computational stability. The minimum grid size, nucleation frequency, and other model parameters remained unchanged. The number of nuclei formed in a specific physical period was observed with varying time steps. To conduct the mesh-independence test for growth velocity and solute concentration at the tip, a single dendrite was nucleated and grew at the center of the computation domain under conditions of $\Delta T_0 = 10$ K and $CR = 2$ K/s.

Figure 2 illustrates the variation in the number of nuclei, growth velocity and solute concentration at the tip across different space and time steps. It is evident that when the space steps vary between 0.5 μm and 2.5 μm, and time steps vary within the range of 0.5 μs and 4.0 μs, the total number of grain nuclei remains unchanged. The tip velocity and concentration generally remain stable, with slight variations within a small range. This indicates that the simulation results of the present model are convergent at different grid resolutions, which ensures the stability, and reliability of the simulation. Furthermore, these results serve as a guideline for selecting appropriate space and time step sizes to maintain a balance between computational accuracy, stability, and efficiency.

Table 1. Physical parameters used in the simulation for Al–Zn–Mg alloys.

Symbol	Definition	Value	References
$T_{\mathrm{m,Al}}$	melting temperature of the pure Al	933.6 K	[32]
$\bar{\Gamma}$	average Gibbs–Thomson coefficient	2.4×10^{-7} m·K	[33]
ε	degree of surface energy anisotropy	0.03	estimated
δ	degree of kinetic anisotropy	0.40	estimated
$\bar{\mu}$	average interface kinetic coefficient	3.0×10^{-5} m/(s·K)	estimated
ρ	density	2920 kg/m^3	[34]
C_{p}	heat capacity	1100 J/(kg·K)	[35]
λ	thermal conductivity	125 W/(m·K)	[34]

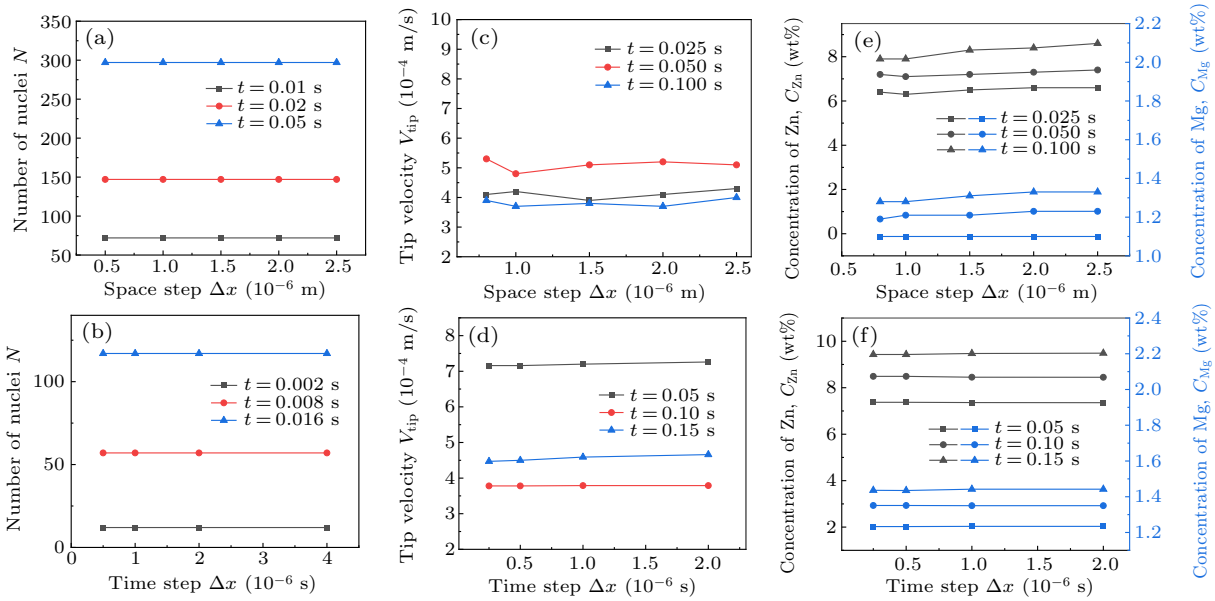


Fig. 2. Verification of mesh independency: (a) number of nuclei at various space steps with fixed time interval, (b) number of nuclei at different time intervals with fixed space steps, (c) tip velocities at various space steps with fixed time interval, (d) tip velocities at different time intervals with fixed space steps, (e) tip concentrations at various space steps with fixed time interval, (f) tip concentrations at different time intervals with fixed space steps.

3.1.2. Comparisons with experimental results

To validate the accuracy of the proposed model, the simulated solidification microstructure of the Al–Zn–Mg alloy was compared with experimentally observed metallographic images of alloys.

Figure 3 illustrates the comparison between the simulation results and experimental observations of aluminum alloy microstructures reported by Zhu *et al.*[36] The white part in

Fig. 3 indicates the solid phase, while the black part is the liquid phase. In the simulation, the temperature field was set to be uniform and initial grain nuclei were randomly placed into the computational domain. The grains started to grow up driven by the initial undercooling of 10 K. During the solidification process, grains continuously nucleate and grow up based on the prevailing temperature conditions. We simulated the grain morphology under two cooling rates of 1 K/s and 10 K/s.

As shown in Fig. 3, the number and size of grains increases progressively throughout the solidification process. At a low cooling rate, the solid phase exhibits a globular morphology. When at a higher cooling rate, a dendritic morphology emerges. This dendritic structure is characterized by variations in size and shape, as well as the development of side branches. The morphological characteristics predicted by the simulation agree well with the experimental observations obtained by Zhu *et al.*[36] and similar dendritic morphologies were also observed by Marsh *et al.*[37] and Spinelli *et al.*[38] It is demonstrated that the proposed model effectively captures the continuous nucleation and grain growth processes in the ternary alloy system. Furthermore, it accurately describes the evolution of grain morphology under varying solidification conditions.

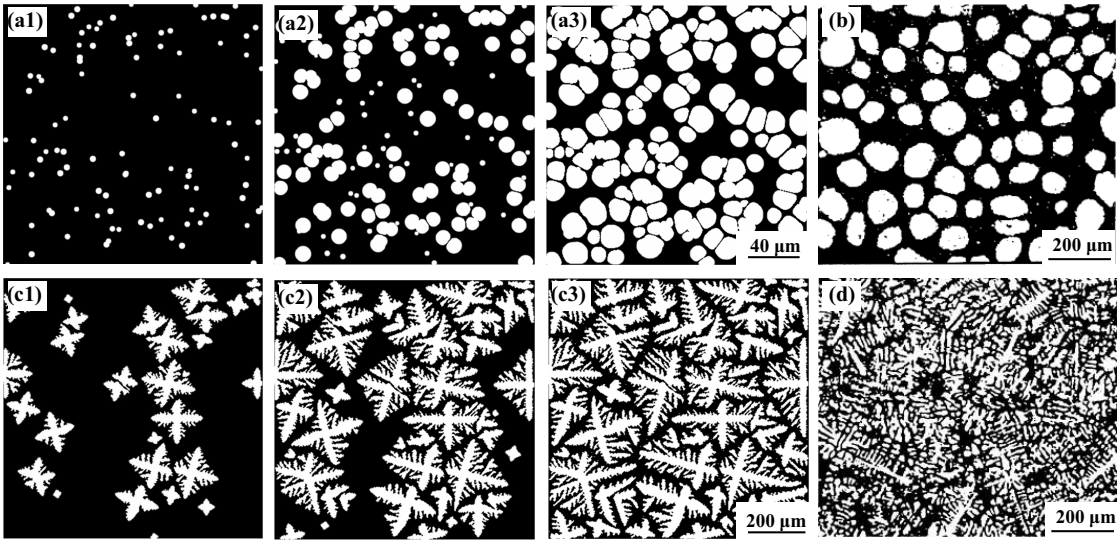


Fig. 3. Simulated and experimental[36] results of solidification microstructure of the Al–Zn–Mg alloy under different processes: (a1) $CR =$ 0.3 K/s, $f_s = 0.02$; (a2) $CR = 0.3$ K/s, $f_s = 0.21$; (a3) $CR = 0.3$ K/s, $f_s = 0.52$; (b) experimental results at $CR = 0.3$ K/s; (c1) $CR = 10.0$ K/s, $f_s = 0.25$; (c2) $CR = 10.0$ K/s, $f_s = 0.43$; (c3) $CR = 10.0$ K/s, $f_s = 0.51$; (d) experimental results at $CR = 10.0$ K/s. Panels (a)–(d) shown in solid fraction.

3.2. Evolution of solidification microstructure

To investigate the microstructure formation and concentration distribution under different conditions, we firstly simulated two solidification processes with typical microstructural features. In the case of traditional solidification of an Al–7 wt% Zn–2.6 wt% Mg alloy, the computational domain was divided into 600×150 cells with a cell size of 5 μm. In the case of the solidification in a melt pool, the calculation area was set to be 560×210 cells with a cell size of 6 μm.

The initial number of nucleation was determined according to the initial undercooling using Eq. (3). The nucleation parameters used are listed in Table 2.[39–41] Nuclei were randomly distributed in regions undercoolings and were assigned random crystallographic orientations.

Table 2. The nucleation parameters used in the calculation.

	n_{max} (m^{-3})	ΔT_{max} (K)	ΔT_σ (K)
Figure 4	3.0×10^{13}	5.0	2.0
Figure 5	9.0×10^{13}	5.0	1.5

Two cases were examined with different thermal boundary conditions and initial temperature distributions. In the first case, the left and right boundaries were treated as mold walls, while in the other case, the bottom boundary was considered a mold wall additionally. Near the mold walls, the molten metal experienced more rapid cooling, starting with an initial undercooling of 20 K. The temperature distribution evolved following the governing equations and the entire computational domain cooled down at a constant cooling rate of $CR = 10$ K/s.

Figures 4 and 5 present the simulation results, showing the microstructure development and Zn and Mg concentration fields. The dendritic solidification process was observed to occur in three distinct zones and stages: (a) chill zone: nucleation and growth of equiaxed dendrites at the wall, (b) columnar zone: growth of columnar dendrites, and (c) equiaxed zone: nucleation and growth of equiaxed dendrites at the center.

At the beginning of the simulation, the area near the mold wall is more susceptible to nucleation due to the lower temperature and greater undercooling in this region. The undercooling is continuously updated based on Eq. (6), leading to a corresponding increase in the number of nuclei at each time

step. During this stage, nuclei form near the wall and grow freely as equiaxed crystals.

As solidification proceeds, equiaxed dendrites dominate the highly undercooled areas near the walls, changing from the liquid phase to the solid phase. In contrast, the central region of the computational domain remains at a relatively high temperature, with insufficient undercooling to initiate nucleation. Consequently, dendrites in the interior grow directionally as columnar crystals along the temperature gradient.

In the later stages of solidification, the undercooling ahead of the solid–liquid (S/L) interface widens as the columnar grains extend further into the melt. Eventually, the undercooling at the columnar front surpasses the threshold required for nucleation, resulting in instability at the S/L interface. This leads to the nucleation and growth of equiaxed dendrites in the central region, blocking the further advancement of the columnar dendrites. This phenomenon, known as the columnar-to-equiaxed transition, marks a critical stage in the solidification process. The solidification is complete when all cells transition from the liquid phase to the solid phase.

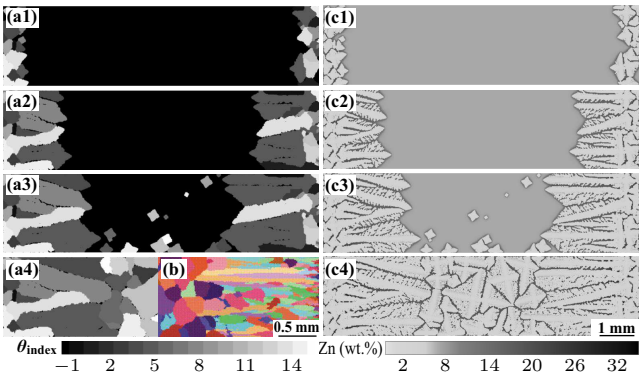


Fig. 4. Simulated evolution of microstructure and concentration of Zn during traditional solidification of an Al–7 wt% Zn–2.6 wt% Mg alloy with $\Delta T_0 = 20$ K, $CR = 10.0$ K/s: (a1) and (c1) $f_s = 0.11$; (a2) and (c2) $f_s = 0.31$; (a3) and (c3) $f_s = 0.49$; (a4) and (c4) $f_s = 0.89$; (b) simulated microstructure of 9SMn28 steel.[42] Panels (a1)–(a4) show in crystallographic orientation index; panels (c1)–(c4) show in the concentration fields of Zn.

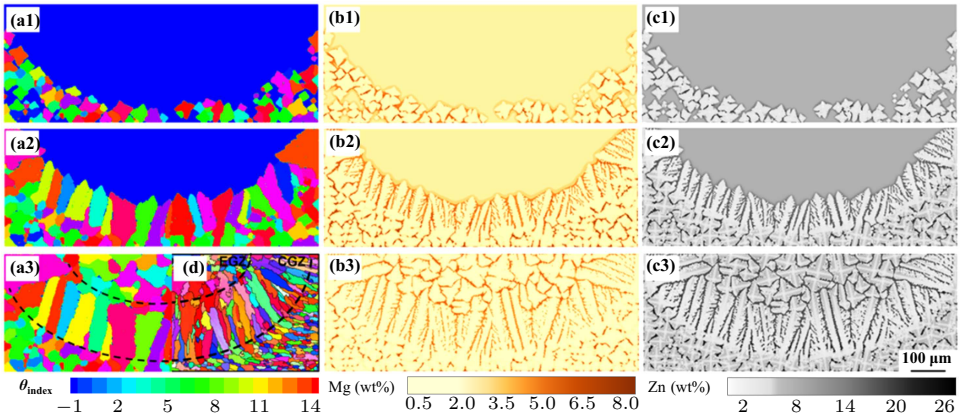


Fig. 5. Simulated evolution of microstructure and concentration of Mg and Zn in a melt pool of an Al–7 wt% Zn–2.6 wt% Mg alloy with $\Delta T_0 = 20$ K, $CR = 10.0$ K/s: (a1), (b1), and (c1) $f_s = 0.20$; (a2), (b2), and (c2) $f_s = 0.44$; (a3), (b3), and (c3) $f_s = 0.88$; (d) experimental micrograph.[43] Panels (a1)–(a3) show in crystallographic orientation index; panels (b1)–(b3) show in the concentration fields of Zn; panels (c1)–(c3) show in the concentration fields of Zn.

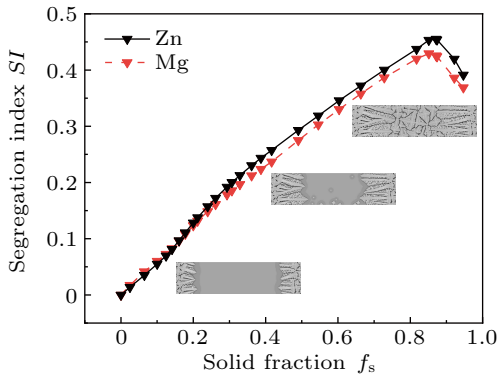


Fig. 6. Simulated solute segregation index versus the solid fraction for the case of Fig. 4.

Additionally, solute segregation can be observed in Figs. 4(c1)–4(c4) and 5(c1)–5(c3). During dendritic growth, solute enrichment occurs near the dendrite tips due to solute rejection at the S/L interface. At the final of solidification, the inter-dendritic regions display markedly higher solute concentrations, highlighting the presence of micro-segregation.

To further investigate the variation in solute segregation during solidification, figure 6 illustrates the relationship between the segregation index SI_i and the solid fraction within the selected region for Zn and Mg. The results in Fig. 6 reveal that the segregation indexes for both solutes increase steadily throughout the early and mid-stages of solidification. Both elements exhibit the same trend of variation, which indicates that solute segregation becomes more pronounced as grains nucleate and grow, leading to local enrichment of element Zn and Mg in the liquid phase. Zn consistently exhibits a higher segregation index than Mg throughout the solidification process. This difference suggests that Zn has a greater tendency for segregation, likely due to its specific partitioning behavior and diffusion characteristics in the Al–Zn–Mg alloy system. The SI_i reaches a peak near a solid fraction of 0.8, after which it decreases slightly as solidification approaches completion. This behavior can be attributed to the dynamic interaction be-

tween solute rejection and diffusion. During early solidification, the expulsion of solute atoms from the solid phase into the surrounding liquid results in the accumulation of solutes near the solid–liquid interface. This enrichment raises the solute concentration in the liquid phase, contributing to an increase in the segregation index. As solidification progresses and the formation of new grains ceases, solute diffusion in the liquid becomes more prominent. This enhanced diffusion gradually homogenizes the solute distribution, bringing it closer to equilibrium. Consequently, the degree of segregation decreases, leading to a slight reduction in the segregation index SI_i during the final stages of the solidification process.

3.3. Effects of initial concentrations

Figure 7 presents the dendritic morphologies and Zn concentration distributions for various initial Zn compositions under a uniform temperature field. The computational domain is divided into a 300×300 grid with a cell size of 3 μm. To isolate the effect of initial Zn composition on the final microstructure, all other parameters remain constant across the simulations. The initial undercooling is set to 15 K, and the cooling rate is fixed at 5 K/s.

It is observed that increasing the initial Zn composition results in more developed dendritic side branches and greater solute segregation between dendrites. At lower initial Zn concentrations (seen in Figs. 7(a)–7(c)), simpler dendritic structures form, characterized by defined primary and secondary arms. These dendrites exhibit larger average grain sizes with stronger primary arms. As the Mg content increases in the alloy's initial composition, secondary dendrite arms become more pronounced. With higher initial Zn concentrations (Figs. 7(c)–7(e)), the primary dendrite arms become thinner and more elongated, while secondary and even tertiary arms grow more extensively, creating increasingly complex dendritic structures. Elevated solute levels exacerbate instability at the solid/liquid interface, further promoting the growth of dendrite arms. Meanwhile, SI_{Zn} increases steadily from 0.28 to 0.53 as the initial alloy composition increases, indicating that solute segregation for Zn intensifies significantly with higher initial Zn content. SI_{Mg} not only increases with the initial Mg concentration but is also influenced by the initial Zn content, suggesting a synergistic interaction between the segregation behaviors of Zn and Mg. Consequently, solute enrichment in inter-dendritic regions becomes more pronounced, leading to significant compositional heterogeneity. These trends are closely related to the partitioning behavior of Zn at the solid–liquid interface that higher Zn concentrations result in a steeper solute concentration gradient in the liquid phase, thereby amplifying the degree of segregation.

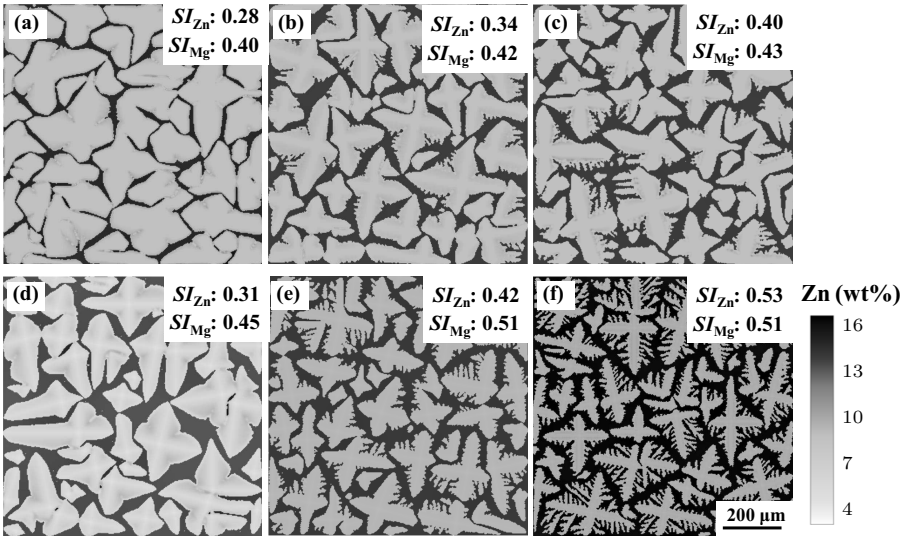


Fig. 7. Simulated dendritic morphologies and concentration fields of element Zn with different initial alloy compositions: (a) Al–5.0 wt% Zn–0.1 wt% Mg; (b) Al–5.0 wt% Zn–1.9 wt% Mg; (c) Al–5.0 wt% Zn–2.6 wt% Mg; (d) Al–2.6 wt% Zn–2.6 wt% Mg; (e) Al–6.7 wt% Zn–2.6 wt% Mg; (f) Al–10.0 wt% Zn–2.6 wt% Mg.

Figure 8 depicts the final solidification microstructure and Zn concentration distribution in a melt pool. The calculation parameters consistent with those used in Fig. 5. This comparison allows for a deeper understanding of how varying initial compositions and thermal conditions influence the evolution of dendritic structures and solute segregation in the alloy. The influence of alloying elements on dendritic morphology and the segregation index in Fig. 8 follows a pattern similar to that in Fig. 7, confirming that solute concentration strongly influences dendritic growth. Besides, figure 8 also demonstrates that the initial alloy composition has minimal effect on the formation of the CET which appears more dependent on thermal conditions than on solute levels.

It is possible that the observed phenomenon arises from the solute rejection process during solidification. As dendrites grow, the solid phase has a lower solubility for solute

atoms, causing these atoms to be expelled into the adjacent liquid phase. This creates a concentration gradient near the solid/liquid (S/L) interface, forming a solute-enriched boundary layer. Solute atoms then diffuse into the bulk liquid from the interface, driven by the concentration gradient.

When the initial solute concentration in the alloy is higher, the solid phase rejects a greater number of solute atoms during dendritic growth. Consequently, the solute concentration in the liquid near the S/L boundary rises significantly. This leads to a steeper concentration gradient at the interface and accelerates the saturation of the liquid's capacity to absorb and redistribute solute atoms. As a result, solute segregation is exacerbated, intensifying heterogeneity in the inter-dendritic regions.

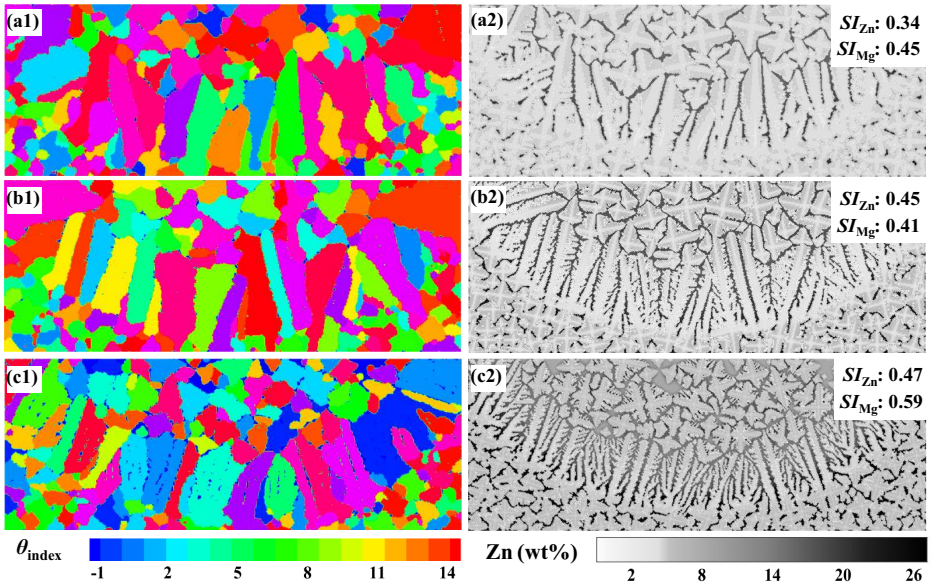


Fig. 8. Simulated microstructure and concentration fields of element Zn with different initial alloy compositions: (a) Al–5.0 wt% Zn–2.6 wt% Mg; (b) Al–7.0 wt% Zn–2.6 wt% Mg; (c) Al–10.0 wt% Zn–2.6 wt% Mg.

3.4. Effects of cooling rates

The cooling rate is widely recognized a key factor in determining the final microstructure. To further investigate the relationship between cooling rate and the evolution of microstructure as well as solute distribution during solidification, the microstructure of an Al–7wt.% Zn–2.6wt.% Mg alloy solidified under an initial undercooling of $\Delta T_0 = 20$ K at varying cooling rates was observed and analyzed.

When the initial temperature within the computational region is uniform, figure 9 presents simulated microstructure morphologies and concentration fields during solidification at cooling rates of $CR = 0.3$ K/s and $CR = 66$ K/s. The results demonstrate that higher cooling rates lead to the development of finer microstructures and more pronounced solute segregation. The concentration distribution of Zn shown in Figs. 9(a) and 9(d) highlights the impact of the cooling rate on solute distribution. At higher cooling rates, Zn segregation becomes more pronounced due to the accumulation of solute in the inter-dendritic regions. This occurs because the restricted diffusion of Zn under rapid cooling conditions increases solute concentration in these areas. Additionally, as shown in Figs. 9(b) and 9(e), the microstructure reveals that higher cooling rates result in finer and more uniform grains. In contrast, lower cooling rates produce larger and more irregular grains, whereas higher cooling rates yield equiaxed grains with a more uniform distribution. The simulation results show strong agreement with the microstructural morphologies observed in experimental studies[44] as shown in Figs. 9(c) and 9(f).

Figure 10 illustrates the simulated microstructure and Zn composition fields under cooling rates of 5 K/s, 10 K/s, 20 K/s, and 40 K/s respectively in a melt pool. The results indicate that higher cooling rates promote the columnar-to-equiaxed transition (CET) and improve solute diffusion.

Figures 10(a) and 10(d) show that as the cooling rate increases, the area of the columnar zone decreases, while the area of the central equiaxed zone expands. The growth direction of columnar grains is determined by the combination of crystallographic orientation and temperature gradient. At a low cooling rate of 5 K/s, the solidification process is slow, allowing for extensive dendrite growth with well-developed primary and secondary dendrite arms. Due to the relatively stable temperature gradients, columnar grains with favorable orientation are favored by the slow cooling rate, growing strongly with side branches all the way to the center with the direction of the maximum temperature gradient. In the central zone, where the temperature is high and the cooling rate is slow, nucleation does not occur due to insufficient undercooling. As the cooling rate increases from 10 K/s to 40 K/s, the dendrites become finer. The microstructure shows a combination of columnar and equiaxed grains as the increased cool-

ing rate promotes nucleation in the central zone while maintaining partial directional solidification. fine-grained structure results from the higher cooling rates, which significantly increase the nucleation rate while shortening the available time for grain formation. The distinction between the columnar and equiaxed zones becomes less clear at higher cooling rates.

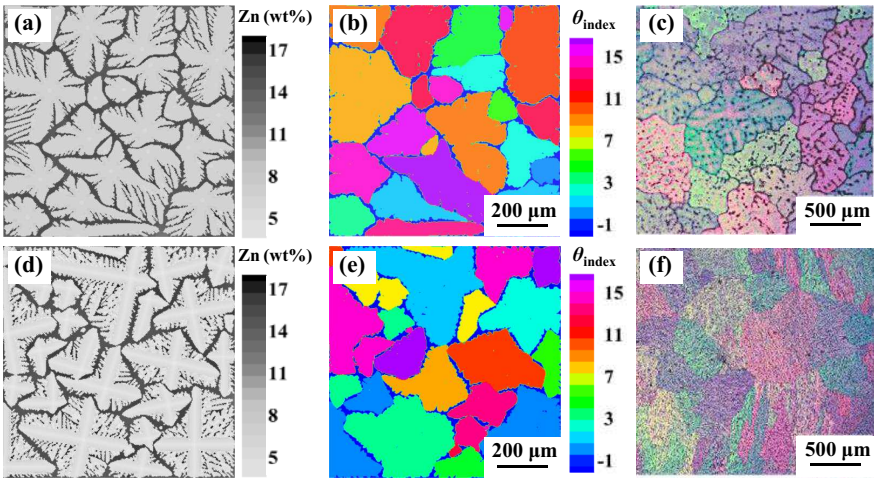


Fig. 9. Simulated and experimental[44] dendritic morphologies and concentration fields of an Al–7 wt% Zn–2.6 wt% Mg alloy at different cooling rates: (a) and (b) simulated results at 0.3 K/s; (c) experimental results at 0.3 K/s; (d) and (e) simulated results at 66 K/s; (f) experimental results at 66 K/s. Panels (a) and (d) show in the concentration fields of Zn; panels (b) and (e) show in crystallographic orientation index.

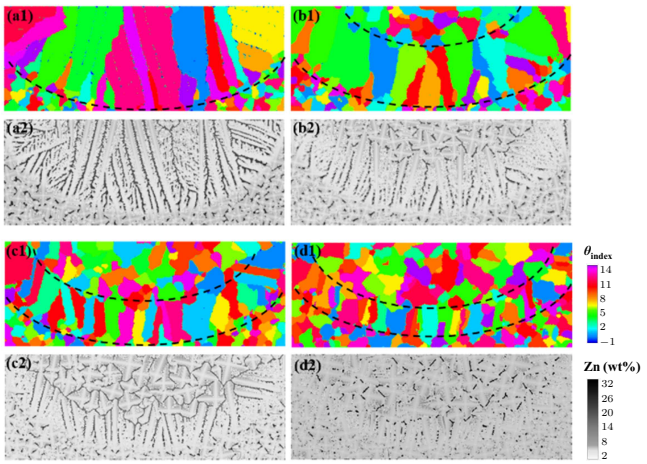


Fig. 10. Simulated morphologies and concentration field of Zn of an Al–7 wt% Zn–2.6 wt% Mg alloy with various cooling rates: (a) 5 K/s; (b) 10 K/s; (c) 20 K/s, and (d) 40 K/s. Panels (a1)–(a4) show in crystallographic orientation index; panels (b1)–(b4) show in the concentration fields of Zn.

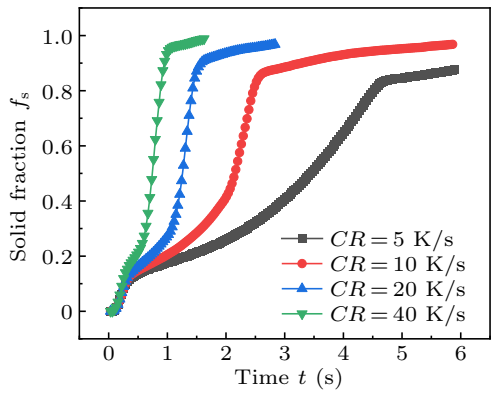


Fig. 11. Simulated solid fraction versus solidification time under different cooling rates.

Figure 11 presents the evolution of the solid phase fraction over time for different cooling rates. The data indicate that higher cooling rates accelerate the increase in the solid phase fraction and significantly shorten the solidification time. In contrast, lower cooling rates slow down the growth of the solid phase fraction, leading to an extended solidification process.

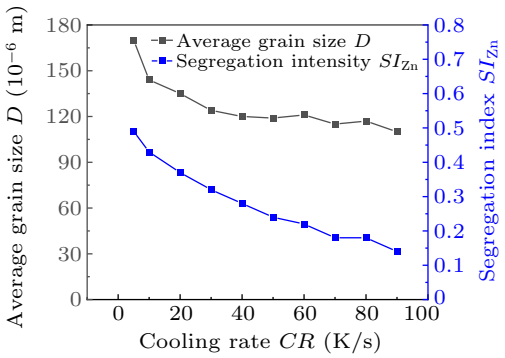


Fig. 12. The effect of cooling rate on average grain size and segregation intensity of Al–7 wt% Zn–2.6 wt% Mg alloy.

Figure 12 depicts the relationship between cooling rates, average grain size, and the segregation index. Combined with the results of Fig. 10, high cooling rate promotes structural refinement and minimizes solute segregation. Specifically, a higher cooling rate accelerates the decrease in domain temperature and provides greater undercooling, significantly increasing the nucleation rate. This leads to the simultaneous formation of a larger number of fine grains, promoting equiaxed grain formation and reducing grain size. Moreover, higher cooling rates shorten the solidification time, limiting the grain growth and solute diffusion in the liquid phase. The cooling rate significantly influences the dynamic behavior of the diffusion process. The rapid solidification induced by higher cooling rates reduces solute partitioning at the solid–liquid in-

terface and limits the formation of concentration gradients in the melt. Additionally, grain refinement decreases dendrite arm spacing with a finer dendritic network, which confines the spatial distribution of solutes within narrower regions and contributes to a greater hindrance to solute diffusion.

4. Conclusion

The CA–FD–CALPHAD coupled model is developed to simulate the solidification microstructures of ternary alloys under various solidification conditions. The evolutions of dendrite microstructure morphologies and solute (Zn and Mg) concentration fields are reproduced and investigated by using this model. The proposed model can accurately reproduce the nucleation and growth of dendrites, and solute redistribution during solidification of Al–Zn–Mg alloys, involving equiaxed and columnar grain growth as well as the columnar-to-equiaxed transition (CET). The simulated morphologies of solidification microstructure agree well with the experimental observations. The microstructure evolution under various initial alloy concentration and cooling rates are studied. The average grain size and segregation index serve as two quantitative indicators for microstructure characteristics. It is found that variations in initial alloy concentration affect both grain morphology and solute segregation. Higher initial alloy concentrations enhance the development of dendritic side branches and more pronounced solute segregation. Besides, increasing the cooling rate significantly influences alloy solidification by refining the microstructure. A higher cooling rate facilitates an earlier transition from columnar to equiaxed growth (CET), while simultaneously decreasing the average grain size. Additionally, higher cooling rates improve solute uniformity by minimizing segregation in inter-dendritic regions.

Acknowledgements

Project supported by the National Natural Science Foundation of China (Grant No. 52301035), the Natural Science Foundation of Jiangsu Province, China (Grant No. BK20230844), and the National Key Research and Development Program of China (Grant No. 2023YFB3710202).

References

[1] Hong C P and Zhu M F 2001 *ISIJ Int.* **41** 43
[2] Paliwal M, Kang D H, Essadiqi E and Jung I 2014 *Metall. Mater. Trans. A. Phys. Metall. Mater. Sci* **45** 3596
[3] Martorano M A and Biscuola V B 2009 *Acta. Mater.* **57** 607
[4] Yan X, Chen S, Xie F and Chang Y A 2002 *Acta Materialia* **50** 2199
[5] Zepon G, Ellendt N, Uhlenwinkel V and Bolfarini C 2016 *Metall. Mater. Trans. A Phys. Metall Mater. Sci.* **47** 842
[6] Jia Y W, Huang H J, Fu Y A , Zhu G L, Shu D, Sun B D and StJohn D H 2019 *Scr. Mater.* **167** 6
[7] Delaleau P, Beckermann C, Mathiesen R H and Arnberg L 2010 *ISIJ Int.* **50** 1886
[8] Nguyen-Thi H, Reinhart G, Mangelinck-Noel N, Jung H, Billia B, Schenk T, Gastaldi J, Hartwig J and Baruchel J 2007 *Metall. Mater. Trans. A Phys. Metall. Mater. Sci.* **38A** 1458
[9] Nestler B and Wheeler A 2000 *Physica D* **138** 114
[10] Zhang A, Yang M H, Qin L, Cheng J, Tang Y C, Du J L, Yu W B, Dong Z H, Liu F, Jiang B and Pan F S 2024 *Comput. Math. Appl.* **176** 289
[11] Zhu C S, Wang T, Feng L, Lei P and Ma F L 2022 *Chin. Phys. B* **31** 028102
[12] Mao S L, Hu M D, Chen W and Sun D K 2024 *Mater. Des.* **246** 113362
[13] Zhang A, Guo Z P, Jiang B, Du J L, Wang C H, Huang G S, Zhang D F, Liu F, Xiong S M and Pan F S 2021 *Acta Mater.* **214** 117005
[14] Eshraghi M, Hashemi M, Jelinek B and Felicelli S D 2017 *Metals* **7** 474
[15] An D, Chen S L, Sun D K Pan S Y, Krakauer B W and Zhu M F 2019 *Comput. Mater. Sci.* **166** 210
[16] Zhang S J, Zhu B F, Li Y B, Zhang Y and Li R 2024 *Comput. Mater. Sci.* **245** 113308
[17] Zhang Y J, Zhou J X, Yin Y J, Shen X and Ji X Y 2021 *J. Mater. Res. Technol.* **14** 1862
[18] Tan Y X, Zhao H D and Xu Q Y 2024 *Sci. China Mater.* **67** 1150
[19] Gu C, Ridgeway C D, Moodispaw, M P and Luo A A 2020 *J. Mater. Process. Technol.* **286** 116829
[20] Liao S H, Webster S, Huang D, Council R, Ehmann K and Cao J 2022 *Addit. Manuf.* **56** 102912
[21] Ramirez A J and Lippold J C 2004 *Mater. Sci. Eng. A* **380** 245
[22] Cook P S and Murphy A B 2020 *Addit. Manuf.* **31** 100909
[23] Chen H R, Liu X, Liu X C and Witherell P 2024 *Addit. Manuf.* **84** 104095
[24] Sheng Y W, Zhou Z Q, Meng X N and Ru J S 2024 *Can. Metall. Q* **0** 1
[25] Xiong F Y, Liang Y P, Panwisawas C, Chen J W, Li M J and Liu A W 2024 *Addit. Manuf.* **95** 104517
[26] An Z, Pan J J, Hu X F and Yang H Y 2025 *Int. J. Heat Mass Transfer* **238** 126452
[27] Chen S L, Daniel S, Zhang F Chang Y A, Yang X Y, Xie F Y, Schmid-Fetzer R and Oates W A 2002 *Calphad* **26** 175
[28] Cao W, Chen S L, Zhang F, Wu K, Yang Y, Chang Y A, Schmid-Fetzer R and Oates W A 2009 *Calphad* **33** 328
[29] Fang H, Tang Q Y, Zhang Q Y, Gu T F and Zhu M F 2019 *Int. J. Heat Mass Transfer* **133** 371
[30] Pan S Y and Zhu M F 2010 *Acta Mater.* **58** 340
[31] Boettinger W J, Warren J A, Beckermann C and Karma A 2002 *Annu. Rev. Mater. Sci.* **32** 163
[32] Hu M D, Sun D K and Zhu M F 2024 *Mater. Des.* **241** 112977
[33] Beltran-Sanchez L and Stefanescu D M 2004 *Metall. Mater. Trans. A Phys. Metall. Mater. Sci.* **35** 2471
[34] Liu T T, Mu Z Y, Hu R Z and Pang S Y 2019 *Int. J. Heat Mass Transfer* **140** 346
[35] Tan C W, Dong Y, Sun H F, Liu F Y, Han X, Dong Q J, Chen B and Song X G 2023 *J. Mater. Res. Technol.* **26** 6446
[36] Zhu M F, Kim J M and Hong C P 2001 *ISIJ Int.* **41** 992
[37] Marsh S P and Glicksman M E 1996 *Metall. Mater. Trans. A Phys. Metall. Mater. Sci.* **27** 557
[38] Spinelli J E, Peres M D and Garcia A 2005 *J. Alloys Compd.* **403** 228
[39] Zhu M F and Hong C P 2001 *ISIJ Int.* **41** 436
[40] Wu M, Li J, Ludwig A and Kharicha A 2013 *Comput. Mater. Sci.* **79** 830
[41] Wu M H, Ludwig A, Bührig-Polaczek A, Fehlbier M and Sahm P R 2003 *Int. J. Heat Mass Transfer* **46** 2819
[42] Wang J L, Wang F M, Zhao Y Y, Zhang J M and Ren W 2009 *Int. J. Miner. Metall. Mater.* **16** 640
[43] Xiong L D, Zhu G L, Mi G Y, Wang C M and Jiang P 2021 *J. Alloys Compd.* **858** 157669
[44] Lu B, Li Y, Wang H Y, Wang Y, Yu W, Wang Z D and Xu G M 2023 *J. Mater. Res. Technol.* **22** 2532